

# Applying Superfluid Helium to Light Dark Matter Searches: Demonstration of the HeRALD Detector Concept

R. Anthony-Petersen,<sup>1</sup> A. Biekert,<sup>1</sup> C.L. Chang,<sup>2</sup> Y. Chang,<sup>1</sup> L. Chaplinsky,<sup>3</sup> A. Dushkin,<sup>4</sup> C.W. Fink,<sup>1</sup> M. Garcia-Sciveres,<sup>5,6</sup> W. Guo,<sup>7,8</sup> S.A. Hertel,<sup>3</sup> X. Li,<sup>5</sup> J. Lin,<sup>1</sup> R. Mahapatra,<sup>9</sup> W. Matava,<sup>1</sup> D.N. McKinsey,<sup>1,5</sup> D.Z. Osterman,<sup>3</sup> P.K. Patel,<sup>3</sup> B. Penning,<sup>4</sup> H.D. Pinckney,<sup>3,\*</sup> M. Platt,<sup>9</sup> M. Pyle,<sup>1</sup> Y. Qi,<sup>7,8</sup> M. Reed,<sup>1</sup> G.R.C Rischbieter,<sup>4</sup> R.K. Romani,<sup>1</sup> A. Serafin,<sup>3</sup> B. Serfass,<sup>1</sup> R.J. Smith,<sup>1</sup> P. Sorensen,<sup>5</sup> B. Suerfu,<sup>6</sup> A. Suzuki,<sup>5</sup> V. Velan,<sup>5</sup> G. Wang,<sup>2</sup> Y. Wang,<sup>1</sup> S.L. Watkins,<sup>1</sup> and M.R. Williams<sup>4</sup>

(SPICE/HeRALD Collaboration)

<sup>1</sup>*University of California Berkeley, Department of Physics, Berkeley, CA 94720, USA*

<sup>2</sup>*Argonne National Laboratory, 9700 S Cass Ave, Lemont, IL 60439, USA*

<sup>3</sup>*University of Massachusetts, Amherst Center for Fundamental Interactions and Department of Physics, Amherst, MA 01003-9337 USA*

<sup>4</sup>*University of Michigan, Randall Laboratory of Physics, Ann Arbor, MI 48109-1040, USA*

<sup>5</sup>*Lawrence Berkeley National Laboratory, 1 Cyclotron Rd., Berkeley, CA 94720, USA*

<sup>6</sup>*International Center for Quantum-field Measurement Systems for Studies of the Universe and Particles (QUP, WPI), High Energy Accelerator Research Organization (KEK), Oho 1-1, Tsukuba, Ibaraki 305-0801, Japan*

<sup>7</sup>*Department of Mechanical Engineering, FAMU-FSU College of Engineering, Florida State University, Tallahassee, FL 32310, USA*

<sup>8</sup>*National High Magnetic Field Laboratory, Tallahassee, FL 32310, USA*

<sup>9</sup>*Texas A&M University, Department of Physics and Astronomy, College Station, TX 77843-4242, USA*

(Dated: July 25, 2023)

The SPICE/HeRALD collaboration is performing R&D to enable studies of sub-GeV dark matter models using a variety of target materials. Here we report our recent progress on instrumenting a superfluid  $^4\text{He}$  target mass with a transition-edge sensor based calorimeter to detect both atomic signals (e.g. scintillation) and  $^4\text{He}$  quasiparticle (phonon and roton) excitations. The sensitivity of HeRALD to the critical “quantum evaporation” signal from  $^4\text{He}$  quasiparticles requires us to block the superfluid film flow to the calorimeter. We have developed a heat-free film-blocking method employing an unoxidized Cs film, which we implemented in a prototype “HeRALD v0.1” detector of  $\sim 10$  g target mass. This article reports initial studies of the atomic and quasiparticle signal channels. A key result of this work is the measurement of the quantum evaporation channel’s gain of  $0.15 \pm 0.012$ , which will enable  $^4\text{He}$ -based dark matter experiments in the near term. With this gain the HeRALD detector reported here has an energy threshold of 145 eV at 5 sigma, which would be sensitive to dark matter masses down to  $220 \text{ MeV}/c^2$ .

## I. INTRODUCTION

Dark matter (DM) models in which the DM mass is between  $1 \text{ keV}/c^2$  and  $1 \text{ GeV}/c^2$  are sometimes termed ‘low-mass DM’, in contrast to DM models based on new physics at the  $>1 \text{ GeV}/c^2$  electroweak scale. Low-mass DM has received increasing attention over the past decade, as it has become clear that these models are cosmologically viable, are only loosely constrained by existing experiments, and retain comparative model simplicity. Such DM models include the ELDER [1, 2], SIMP [3, 4], and ‘freeze-in’ [5] frameworks. These models are testable through direct detection, either via electron scattering or nuclear scattering processes. In the nuclear recoil case, deposited recoil energy scales with the square of the DM mass. To set the energy scale, even for the relatively low-mass target nucleus of  $^4\text{He}$  and a DM mass relatively high in the light-DM range ( $10 \text{ MeV}/c^2$ ), the recoil endpoint energy will be  $\sim 100 \text{ meV}$ . These sub-eV

recoil energy signatures motivate the development of new sensor technologies which is at the core of the TESSERACT R&D program, in which Transition Edge Sensors (TESs) are being advanced to sub-eV phonon-sensing thresholds, and are being applied to a variety of target materials with diverse and complementary DM sensitivities. The  $^4\text{He}$  portion of the TESSERACT program is termed ‘HeRALD’ (Helium Roton Apparatus for Light Dark matter) [6].

### A. Superfluid $^4\text{He}$ as a target material

Superfluid  $^4\text{He}$  offers several advantages over other DM target materials. First, the nuclear mass is comparatively low, which correspondingly boosts the nuclear recoil spectrum endpoint energy. The recoil endpoint scales inversely with atomic mass  $A$ , meaning  $^4\text{He}$  will expect a  $\sim 7\times$  ( $\sim 33\times$ ) increase in endpoint energy relative to Si (Xe).

We also expect the backgrounds in the sub-eV range to be comparatively low.  $^4\text{He}$  is extremely radiopure at mK temperatures, as all impurities freeze out to the bound-

\* Corresponding author: hpinckney@umass.edu

aries. Additionally, the first electronic excited state of  $^4\text{He}$  requires 19.8 eV, meaning Compton scattering processes are entirely forbidden in the wide 0-19.8 eV energy range key to low-mass DM sensitivity. Further, while crystal lattices typically contain dislocations and stress which can lead to spontaneous phonon emission even at zero temperature [7–10], a superfluid material should minimize such stored potential energies and the spontaneous phonon backgrounds arising from them.

Yet another advantage of  $^4\text{He}$  as a DM target material is the variety of unique signal channels: quasiparticle-induced “quantum evaporation”, and electronically-excited dimers. In this context, “quasiparticle” describes a range of phonon-like excitations of the superfluid medium, ranging from low-momentum phonons to higher-momentum  $R^-$  and  $R^+$  “rotons”. The quantum evaporation signal is produced when single  $^4\text{He}$  quasiparticles liberate single  $^4\text{He}$  atoms from the liquid surface in a one-to-one process, sending them into the vacuum above. While this process has an 0.62 meV threshold, if the liberated atoms are sensed calorimetrically then the signal energy is not the atoms’ comparatively small kinetic energy, but instead the much larger van der Waals potential of  $^4\text{He}$  adsorption at the calorimeter surface: roughly 10 meV per atom [11]. A coincidence requirement on multiple quantum evaporation sensors observing a single  $^4\text{He}$  target can allow for a powerful rejection of instrument-related backgrounds.

Particle interactions greater than 19.8 eV also produce electronic excitations. These excitations lead to the formation of  $\text{He}_2^*$  dimers which (as in other liquid noble elements) appear in either a short-lived singlet state (<10 ns) or a long-lived triplet state (13 s) [12–14]. While the singlet excimers decay promptly to emit  $\sim 15.5$  eV VUV photons, the triplet excimers either decay promptly at the recoil site through Penning ionization, or propagate ballistically through the bulk superfluid, de-exciting at surfaces. For more detail on these signal channels and the HeRALD concept, see Ref. [15].

The dual-signal readout of  $^4\text{He}$  in both quasiparticles (via quantum evaporation) and scintillation has been previously explored experimentally by the HERON collaboration [16, 17]. While the original motivation of the HERON program was the detection of pp solar neutrinos via keV-scale electron recoils, the application to DM direct detection via nuclear recoils was also considered [18].

## B. Superfluid film-stopping

$^4\text{He}$  offers numerous advantages as an active medium, however its superfluid nature also poses practical challenges [19]. First, the target and sensors must be contained within a detector of extreme hermeticity. More challengingly, a superfluid  $^4\text{He}$  film typically covers all surfaces within such a closed container [11, 20]. The presence of a  $^4\text{He}$  film on a calorimetric sensor would significantly degrade the sensor’s performance, first by

adding additional heat capacity and energy escape mechanisms, and second by negating the highly advantageous van der Waals gain mechanism. The HERON collaboration prevented film flow to the sensor by implementing a “film-burner”, in which some region of the cell is heated, interrupting the film flow to the calorimeter via evaporation [21]. While successfully demonstrated, the film burner strategy introduces some unavoidable heat-load to the calorimeter itself, raising the sensor’s energy threshold. Given that energy threshold is the main design driver for the HeRALD program, we investigated alternative *heat-free* technologies for film stopping. One method, the “knife-edge” method, has been well demonstrated at higher temperatures, but it was found to be ineffective in our experimental configuration (see Appendix A).

It has been predicted [22] and subsequently demonstrated [23–25] that superfluid  $^4\text{He}$  films do not wet unoxidized cesium. Non-wetting by  $^4\text{He}$  is an extremely rare material property, specific only to the heaviest alkali metals (perhaps only cesium and rubidium). To implement a cesium-based film-stopping method we deposit a cesium film on a region of the cell between the superfluid target and the sensor used for scintillation and evaporated atoms. To avoid oxidation, this cesium deposition must occur *in situ* within the detector during the cool-down. Implementation of this approach is described in Sec. II and Appendices A and B.

## C. HeRALD v0.1

This article summarizes work with a prototype HeRALD detector, which we term v0.1. The goal of this prototype was to observe particle interactions in a superfluid  $^4\text{He}$  target using a single sensor, suspended in the vacuum over the target and kept dry by a cesium-based film stopper.

## II. DETECTOR SETUP, CESIUM TESTING, AND DATA COLLECTION

### A. The HeRALD v0.1 Detector

To accomplish the goals of HeRALD v0.1 we assembled the detector system illustrated in Fig. 1, referred to as the “cell”. This cell is accompanied by a number of cryostat systems described in Appendix A.

At the heart of the detector system is the  $^4\text{He}$ -free (dry) “sensor platform” which supports a large-area calorimeter above the target  $^4\text{He}$  volume. This sensor is a recent iteration of the ‘Cryogenic Photon Detector’ [26, 27], based on a 3-inch-standard Si wafer of 1 mm thickness. The upper surface of the wafer is instrumented to sense athermal Si phonons using an array of tungsten transition-edge sensors (TESs) with a critical temperature of 51 mK. Athermal phonons in the silicon substrate are absorbed by aluminum fins, which transport

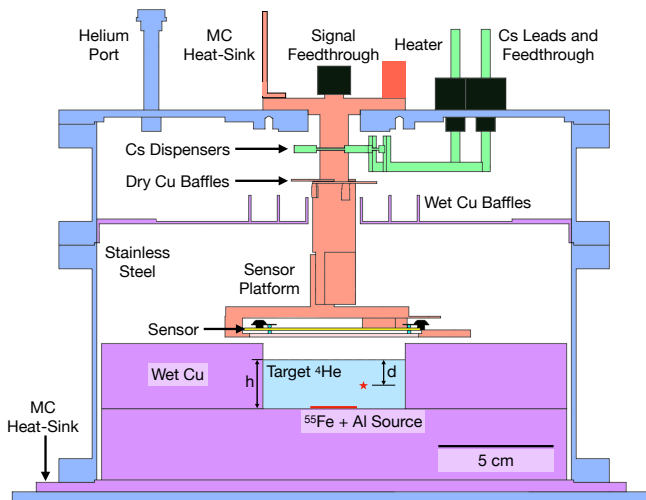


FIG. 1. Annotated cross section of the detector used in this work. The  $^4\text{He}$ -wetted surfaces are the stainless steel cell boundaries (blue), the copper shielding plates (purple), and the cesium dispensers (green). The  $^4\text{He}$ -free “dry” surfaces are suspended from the cesium region: the sensor platform (orange), the silicon “3-inch-standard” calorimetric sensor itself (yellow), and the sapphire ball detector clamps (light blue). The target  $^4\text{He}$  volume is represented as light blue. As referenced in the text, the total  $^4\text{He}$  fill height “ $h$ ” and the depth of an interaction “ $d$ ” are defined as indicated. An X-ray source at the bottom of the  $^4\text{He}$  target region is also indicated.

the energy into the TESs in a standard “QET” type architecture [28]. The 673 TESs are connected in parallel as a single channel. After fabrication, a single TES was disconnected from the array and repurposed as a resistive heater. The calorimeter is mechanically secured to the sensor platform using three sapphire-ball-based clamps [29]. In each of the three clamps, the wafer is pressed between two 1.5 mm diameter sapphire balls using one hard-temper phosphor bronze spring. A weak thermal link between the calorimeter and the platform is constructed using a gold pad and a gold wirebond. The sensor array and heater are connected electrically via aluminum wire bonds to superconducting PCBs on the platform, which in turn connect to NbTi twisted pairs. These twisted pairs exit the experimental cell through a Stycast 2850FT feedthrough. The sensor platform has a dedicated thermal link to the mixing chamber stage consisting of two copper (grade 101) sheets in parallel, each being 3 cm wide  $\times$  10 cm long  $\times$  0.5 mm thick. A thermometer and resistive heater were secured to the sensor platform structure on the outside of the cell.

Directly below the sensor platform is the  $^4\text{He}$  target region: a 2.75 cm high, 6 cm diameter cylinder. This region is defined by two copper plates which also provide some shielding of the region from external gamma backgrounds. We will refer to the amount of  $^4\text{He}$  in this region by its fill height “ $h$ ”, and separately the depth of

an interaction relative to the  $^4\text{He}$  surface as “ $d$ ”. The  $^4\text{He}$  enters this target volume through a 1.7 mm ID, 2.1 mm OD capillary connected via a VCR flange on the top of the cell.

The calibration source is immersed within the target  $^4\text{He}$  volume and consists of  $^{55}\text{Fe}$  on a thin copper substrate, laminated with  $\sim 75\ \mu\text{m}$  of polypropylene, and covered with a  $\sim 25\ \mu\text{m}$  thick layer of Al. The dominant X-ray produced by  $^{55}\text{Fe}$  is 5.9 keV. We expect a 5.9 keV electron-recoil-like event to deposit 24% (1400 eV), 32% (1875 eV), and 34% (1975 eV) of the recoil energy into the triplet excimer, singlet excimer, and quasiparticle channels of the detector respectively, with the remainder (10%) appearing as infrared radiation. These partitions were estimated using a simulation code which implements the scintillation yields from [30] and is inspired by the NEST package [31, 32]. A higher-energy X-ray at 6.5 keV is also produced, but at lower flux (lower by a ratio of 1:7.3). The Al layer is added specifically to produce a useful fluorescence X-ray at 1.5 keV. The source activity was  $\sim 140\ \text{Bq}$ , corresponding to a rate of  $\mathcal{O}(100)$   $^{55}\text{Fe}$  events per hour in the target  $^4\text{He}$ . In addition to providing calibration peaks at 5.9 and 1.5 keV, these two X-ray energies exhibit distinct path lengths in the superfluid: 0.4 cm at 1.5 keV and 25 cm at 5.9 keV. This difference in path length allows us to have two different populations under study: one concentrated at the bottom center of the  $^4\text{He}$ , and another more uniformly distributed throughout the target.

The cesium-based film stopping system occupies the upper region of the cell as illustrated in Fig. 1. Four commercial cesium dispensers<sup>1</sup> evaporate a Cs vapor when heated using several Amps of current. These dispensers are arranged in a ring and are mechanically supported only by their two copper current leads, which enter the cell via a second Stycast 2850FT feedthrough. To avoid Cs deposition on the sensor itself, copper baffling prevents any line-of-sight path between the dispensers and the sensor.

All of these systems are contained within a surrounding stainless steel experimental cell. The cell is sealed using indium and is supported structurally from its base. The structural support also serves as a thermal link between a copper base plate (which forms a portion of the cell interior) and the mixing chamber stage.

## B. Cesium Efficacy

The deposition of the cesium film begins with the cell surfaces at  $\sim 4\ \text{K}$ . A current is applied to the commercial cesium dispensers, ramping up to 7.5 A (a dispenser temperature of  $\sim 800\ \text{°C}$ ). This heats the sensor portion of the cell to  $\sim 70\ \text{K}$ . After deposition, the cesium current

<sup>1</sup> CS/NF/3.9/12 FT10+10 from SAES

leads are mechanically disconnected within the vacuum space before the cooldown continues to a  $\sim 7$  mK base temperature. More details are presented in Appendix B.

Before condensing  $^4\text{He}$  within the cell, the calorimeter is characterized in a  $^4\text{He}$ -free state. Condensation proceeds via a 20 sccm flow from room temperature within the capillary. While the majority of  $^4\text{He}$  arrives at the detector already condensed within the capillary as a superfluid, it is observed that some  $^4\text{He}$  arrives at the detector in a gas phase, thereby wetting the sensor platform region and necessitating a post-fill bake of the sensor platform to remove this film. Short-duration (2 second) heat pulses are applied first to the sensor platform and then directly to the Si wafer through the TES heater removed from the array. The heat pulse to the platform raises both the platform and silicon to 1 K, and the heat pulse to the silicon raises the Si temperature to  $\sim 1$  K while keeping the platform below 500 mK (Si temperature estimated through thermal modeling). This high Si temperature is required in order to remove the last atomic layer of  $^4\text{He}$ , and is achievable due to the engineered thermal conductance between the sensor and mixing chamber. If the cesium system is working, we should see that no  $^4\text{He}$  re-enters the sensor platform following these heat pulses.

The effect of this  $^4\text{He}$  removal procedure is shown in Fig. 2, where the times of three heat-pulse series are indicated with vertical red lines on the bottom panel. The amount of  $^4\text{He}$  film present can be estimated using the Si phonon transport efficiency, monitored using a calibration X-ray peak at 5.9 keV. Energy dissipated in the TES can be inferred from the pulse integrals (the electrothermal feedback integral method of Ref. [33]), and in Fig. 2 we show the 5.9 keV signal response over the course of this example baking procedure. The upper panel shows the 5.9 keV spectral peak as it appears in the detector before filling (meaning no  $^4\text{He}$ ), after filling, and after baking. The lower panel tracks the 5.9 keV peak signal amplitude throughout the filling and baking procedure. Horizontal ranges indicate the time window used to estimate the 5.9 keV response, and error bars in the energy axis represent an uncertainty in TES bias. Following the  $^4\text{He}$  fill, the signal amplitude is noticeably suppressed. Baking steps are seen to increase the signal amplitudes to an asymptotic higher value, in fact exceeding that of the earlier dry state (when the signal was slightly suppressed due to a slightly higher Si temperature). We see this new higher signal amplitude remains constant over at least a days-long timescale, indicating that the cesium film has succeeded in blocking the flow of superfluid  $^4\text{He}$  to the sensor.

### C. $^4\text{He}$ Data Collection

The data presented here includes measurements at several  $^4\text{He}$  fill states. After each  $^4\text{He}$  fill and subsequent sensor bake, the sensor cools sufficiently for data-taking within a 1 h timescale. We recorded data at six fill

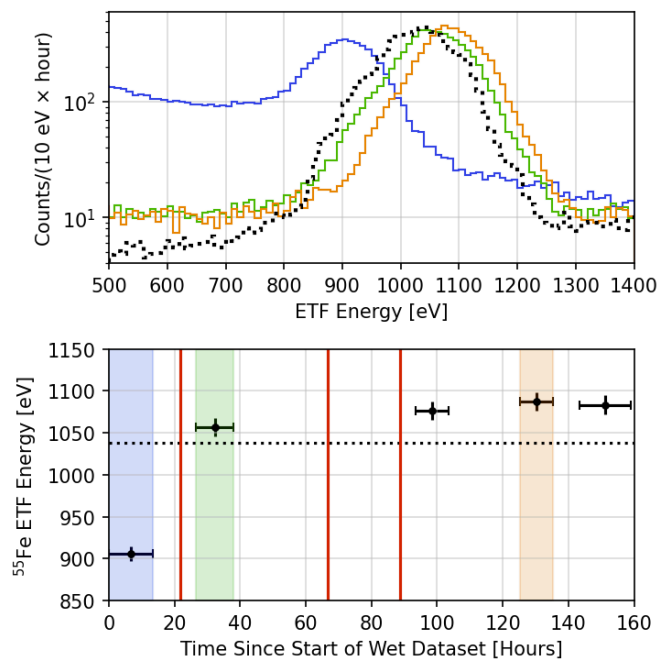


FIG. 2. A sensor baking procedure to remove the  $^4\text{He}$  film, demonstrating the efficacy of the cesium-based superfluid-film blocking system. *Top*: four spectra in the region of the  $^{55}\text{Fe}$  X-ray peak: (black dotted) no  $^4\text{He}$ , (blue) after filling  $^4\text{He}$ , (green) after initial bakes, and (orange) after additional bakes. *Bottom*: The reconstructed peak energy of the  $^{55}\text{Fe}$  X-ray source interacting with the silicon sensor, where the peak energy is computed with the electrothermal feedback (ETF) integral method from [33]. Vertical red lines indicate detector heating. Shaded color bars highlight the time period for the later three spectra. The horizontal black dotted line indicates the dry state peak height. Horizontal error bars represent the span of the data set used to compute the peak amplitude, and error bars in energy represent an uncertainty in bias point.

heights:  $h = 9$  mm, 13 mm, 19 mm, 22 mm, 25 mm, 27.7 mm. These fill heights are determined using the pressure drop in the room temperature  $^4\text{He}$  storage tank and the measured detector dimensions. The final fill height is estimated to be  $\sim 0.2$  mm over-full (filled over the top of the copper plate, but not in contact with the sensor platform) and showed a sudden increase in low-energy event rate (presumably due to the new large area of  $^4\text{He}$  with a poor geometry for signal collection). The fill height uncertainty is approximately  $\pm 2$  mm.

Sensor waveform data was shaped by a 500 kHz low-pass anti-aliasing filter and recorded as a continuous datastream at 1.25 MHz, see Appendix A. Event finding occurred in subsequent offline analysis (described in Sec. III). Data was recorded at each fill height for  $\mathcal{O}(10)$  h. Beginning with the  $h = 22$  mm data set the cryostat was surrounded with a water tank of  $\mathcal{O}(10)$  cm thickness to further reduce the rate of background Compton scattering by a factor of 2.

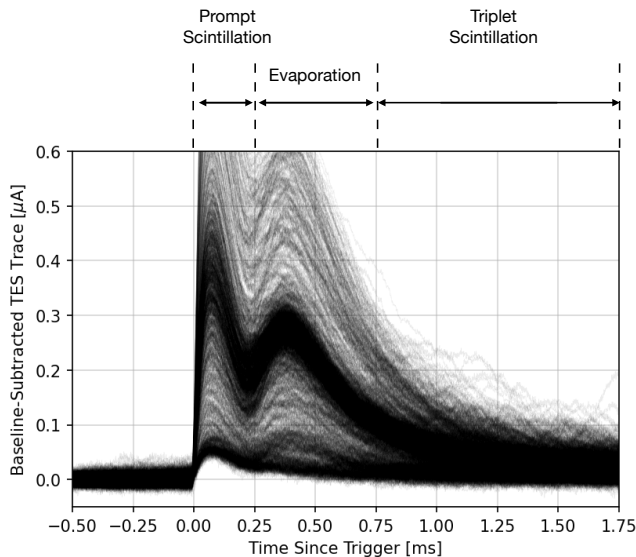


FIG. 3. Overlay of many  $^4\text{He}$  waveforms of the  $h = 13$  mm data set (baseline subtracted). Scintillation, then evaporation, then triplet-dominated time windows are visible. The X-ray calibration features at 5.9 and 1.5 keV are visible as denser bands (with evaporation amplitudes at  $\sim 0.27 \mu\text{A}$  and  $\sim 0.08 \mu\text{A}$ ). Waveforms for this plot are selected using the standard quality cuts described in Sec. III, together with a 40 eV energy threshold on the first pulse. We also enforce that the event occurs in the  $^4\text{He}$  by requiring an evaporation delay in the observed range of 150-250  $\mu\text{s}$ , and we select both using a general  $\chi^2$  metric and a  $\Delta\chi^2$  difference between a single-pulse and double-pulse fit.

### III. DATA PROCESSING, DATA SELECTION, AND CALIBRATION

#### A. Particle Interactions in $^4\text{He}$ and Data Processing

The several signal channels of  $^4\text{He}$  are separated in arrival time at the calorimeter. Figure 3 shows many  $^4\text{He}$  events from one fill state ( $h = 13$  mm). We identify three time intervals within each waveform:

1. Prompt scintillation arrives nearly instantaneously with the recoil itself ( $t = 0$  ms) with a pulse rise and fall determined by the Si phonon collection within the calorimeter.
2. Quantum evaporation arrives over a broader time after a delay of  $\mathcal{O}(100 \mu\text{s})$ .
3. The quenching of the triplet molecules at  $^4\text{He}$  interfaces dominates the waveform at late times ( $t > 0.75$  ms), although some level of triplet quenching within the recoil track likely occurs earlier.

Events are analyzed using an optimum filter (OF) framework applied to the data in two steps. First, events

are found using a single-pulse OF, utilizing the scintillation pulse shape as the signal template. The event finding procedure saves traces of 5 ms length. After event finding, each waveform is passed through a two-pulse OF which simultaneously identifies the amplitude of the scintillation and evaporation pulses as well as their start times. The key outputs of this algorithm are a fitted prompt scintillation amplitude, a fitted evaporation amplitude, and the fitted time difference between the two pulses.

For construction of the OF, we estimate the power spectral density of the noise using traces at randomly selected times. The purity of this noise sample was improved using selection criteria on the baseline average, baseline slope, baseline standard deviation, “general” (single-pulse)  $\chi^2$ , integral-estimated energy, and a pileup event amplitude. The scintillation pulse template for the OF was assembled by “stitching” two pieces: the rising portion of the pulse was taken directly from averaged  $^4\text{He}$  scintillation waveforms, while the falling portion was taken from events where energy was deposited directly into the Si of the calorimeter. This stitching of rising and falling portions was performed in order to capture any true effect of  $^4\text{He}$  scintillation light timing at early times, and to avoid contamination at later times from the overlapping evaporation signal. This scintillation shape was observed to be consistent between data sets.

With the scintillation pulse template now constructed, the evaporation pulse template for the OF was constructed from residuals after scintillation-only fits, with each evaporation-dominated residual waveform shifted according to a fit for the evaporation pulse start time. We find that evaporation pulse shapes show some level of variation, shown in Fig. 4 and discussed in Sec. IV A. For simplicity in the formation of an OF for amplitude and delay time estimation, we choose a single “typical” evaporation waveform (the average evaporation waveform for  $h = 22$  mm data) to play the role of the evaporation signal template in the OF processing of all data. The slight mismatch between this “typical” evaporation waveform and any specific waveform introduces some systematic error in the OF amplitude estimator. We quantify this systematic error by applying a varied choice of OF template waveform to the same data, and find that the systematic error on estimated evaporation amplitude is less than  $\sim 5\%$  throughout this analysis.

#### B. Data Selection

Throughout this work a number of standard selections are applied to the data. In order to ensure that we are measuring interactions in a quiescent detector we remove outliers in pre-pulse baseline average, baseline slope, and baseline standard deviation. To select events specifically within the  $^4\text{He}$  (as opposed to the Si), we select in evaporation time delay. This selection is conservatively loose,

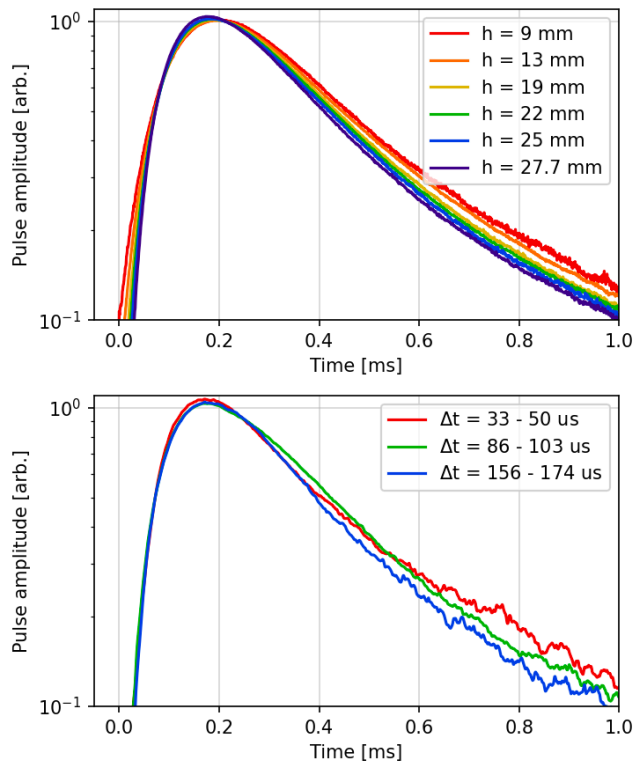


FIG. 4. Residual evaporation pulse shapes after subtracting off the scintillation component. *Top*: median pulse shapes for a variety of fill heights, considering the entire experimental volume. *Bottom*: partial-volume median pulses (top/middle/bottom of the  ${}^4\text{He}$ ) at one fixed fill height ( $h = 27.7$  mm). The evaporation shape is observed to change as a function of both “ $h$ ” and “ $d$ ”. In each panel,  $t = 0$  marks the start of the evaporation pulse as determined by the optimal filter.

above and below the clear “interactions in  ${}^4\text{He}$ ” band for each fill level (see Figs. 6 and 7). Also, unless otherwise stated, we use the term “general  $\chi^2$ ” to refer to a  $\chi^2$  selection using a single-template OF fit, and “ $\Delta\chi^2$ ” to refer to a selection based on the difference in  $\chi^2$  between a two-template and single-template OF fit. Each of these selections removes electronic noise events and helps to ensure we are only considering interactions in the target region. The  $\Delta\chi^2$ -based distinction between Si ‘direct hits’ and  ${}^4\text{He}$  ‘double pulses’ becomes challenging near threshold, where we approach the noise floor of the sensor and also the single-detected-photon limit of the scintillation signal.

In certain analyses we also apply an amplitude selection for  ${}^{55}\text{Fe}$  events in  ${}^4\text{He}$ . This selection is trapezoidal in the space of delay time vs. prompt scintillation energy of Fig. 7, and is again defined to be conservatively loose, to ensure inclusion of the full  ${}^{55}\text{Fe}$  distribution.

## C. Calibration

The detector energy scale is calibrated using the 1.5 keV Al fluorescence peak appearing directly in Si in pre- ${}^4\text{He}$  data. For the specific analyses of this work, the calibration data was obtained from the previous cooldown of the experiment, leading to a 6% systematic uncertainty on this calibration (estimated using the lower-rate 1.5 keV flux reaching the Si at the lowest  ${}^4\text{He}$  fill state of this cooldown). From the 1.5 keV peak, the collection efficiency of Si phonon energy into the TES system is found to be 26%. We assume a linear calibration between this 1.5 keV energy and 0 eV, informed using pulse shape comparison.

An additional correction is made to account for detector state variation throughout the multiple-week data-taking period. The reference point for these corrections is the  ${}^{55}\text{Fe}$  scintillation peak from the bottom-most portion of the  ${}^4\text{He}$  target region. This bottom-most portion of the  ${}^4\text{He}$  is particularly high in rate (see Fig. 6) due to additional contributions from Auger electron emission by the source. We adjust the energy scales of each dataset by at most 6% to counter observed variation in the median of this scintillation peak from this region of  ${}^4\text{He}$ .

The result of the calibration effort is an estimate of energy deposited into the athermal phonon system of the Si: “eV<sub>Si</sub>”.

## IV. DETECTOR PERFORMANCE STUDIES

### A. Evaporation Pulse Shapes

While a single “typical” evaporation pulse shape was chosen for the OF analysis, the observed evaporation pulse shapes in Fig. 4 show small but important variations. The evaporation shapes are estimated by taking the residual of the prompt template fit and iteratively determining the median at each time bin. The traces in Fig. 4 are the time series of these iteratively determined medians. The evaporation signal is broader when the fill height is low, indicating a greater dispersion in the evaporated atom arrival time. This is a result of the larger vacuum gap and the signal timing being dominated by the atomic propagation in the vacuum: compared to the quasiparticle propagation the atoms are slower (by roughly a factor of 2), and have greater velocity and angle (path length) dispersion, which each act to extend the pulse duration.

Pulse shape variation is also seen in the falling edge when comparing evaporation waveforms from different interaction depths. On this falling edge we identify the presence of potential “quasiparticle echo” features, where quasiparticles could be reflecting from the bottom and sides of the target volume. In the 27.7 mm fill state shown in the lower panel of Fig. 4, events near the top of that volume appear to show a small feature at  $\sim 0.4$  ms. This faint feature matches expectation in timing for an

echo off the bottom of the target region, given a two-way quasiparticle travel distance of  $\sim 50$  mm and a quasiparticle group velocity of  $\mathcal{O}(200$  m/s).

### B. Scintillation and Evaporation Amplitudes

In this and the following subsections, we employ the two-template optimal filter processing described in Sec. III to highlight observations regarding the evaporation and prompt scintillation amplitudes, and the delay times between the two signals.

After each waveform is processed to extract amplitude estimates of the evaporation and prompt scintillation components individually, the two amplitudes can be plotted on an event-by-event basis, as in Fig. 5 (left panel). In this analysis, we apply selections on the baseline parameters, evaporation delay time, and  $\Delta\chi^2$ . This left panel is specifically for the  $h = 22$  mm fill state. The 5.9 keV calibration peak appears well above threshold in both signal channels. In prompt scintillation, the peak appears as  $\sim 350$  eV<sub>Si</sub> of energy in the Si. We expect the energy of an electron recoil signature in  $^4\text{He}$  to be partitioned roughly equally among singlet excimers (scintillation), triplet excimers, and quasiparticles. More precisely, for a 5.9 keV deposit we expect  $\sim 1875$  eV of energy in the singlet channel, the dominant producer of prompt scintillation [30]. The observed  $\sim 350$  eV<sub>Si</sub> scintillation signal amplitude is consistent with that  $\sim 1875$  eV expectation given the solid angle of the calorimeter (between 15% and 40%). This work is not yet of sufficient precision to comment on contributions to the prompt signal from either prompt triplet deexcitation (via Penning ionization) or IR photons from higher excited states. These topics will be the focus of future investigations.

The 1.5 keV calibration peak is also observed in Fig. 5 (left panel), appearing near threshold with scintillation energy of  $\lesssim 170$  eV<sub>Si</sub>. At 1.5 keV, the mean observed number of 15.5 eV scintillation photons will be  $\sim 5$ , explaining the observed large variance on the 1.5 keV scintillation signal amplitude.

In the evaporation channel, we see the 5.9 keV energy deposit appears as  $\sim 300$  eV<sub>Si</sub> of energy in the Si of the calorimeter. Again understanding that electron recoil energy is partitioned roughly equally in  $^4\text{He}$  between singlet excimers, triplet excimers, and quasiparticles, we estimate this  $\sim 300$  eV<sub>Si</sub> corresponds to  $\sim 1975$  eV of initial quasiparticle energy, or a quasiparticle channel gain of  $0.15 \pm 0.012$ , where the uncertainty comes from combining the calibration uncertainty with the evaporation pulse shape mismatch (variation) systematic in quadrature, and we do not include an uncertainty on the model. This evaporation channel gain combines multiple effects, in particular the evaporation efficiency (fraction of  $^4\text{He}$  quasiparticles which lead to evaporation) and the van der Waals gain (energy per  $^4\text{He}$  atom adsorbed onto the Si surface). While it is difficult to separately measure these two effects, if we assume a van der Waals gain of

10 meV/atom, then the observed 0.15 gain implies an evaporation efficiency of 1-2%. This small evaporation efficiency emphasizes the importance of van der Waals gain to the technology's viability: it takes a small number of evaporated atoms and converts those atoms to a sizeable calorimetric signal.

It is instructive also to study the evaporation and prompt scintillation amplitudes as the  $^4\text{He}$  fill height is varied. This variation is shown for the  $^{55}\text{Fe}$  peak in Fig. 5 (right panel). Here we apply selections on the baseline parameters, delay time, general  $\chi^2$ , and  $\Delta\chi^2$ . After loosely selecting the  $^{55}\text{Fe}$  peak region, we construct event density contours to highlight the extent of the peak. The event density is normalized by live-time at each fill state, and for each fill state a contour is constructed at 0.0125 counts/(eV<sub>Si</sub><sup>2</sup>-hour). We see that as the fill level increases, the mean signal amplitudes (in both channels) increase due to solid angle effects. The evaporation signal evolves with fill state in a more complex way, because evaporation is dominated by quasiparticles close to normal incidence with the liquid surface ( $\lesssim 17^\circ$ ). This restriction to a narrow cone of quasiparticles leaving the interaction leads to a roughly depth-independent number of evaporated atoms. This said, atoms are evaporated from the surface with a full  $2\pi$  range of outgoing solid angle, meaning atomic transport efficiency is highly sensitive to the geometry and thickness of the vacuum gap, and can play an important role in evaporation signal gain even for events near the bottom surface.

### C. Time Delay Distributions and Interaction Depth

The distribution of evaporation signal delay times can be studied to better understand the physics of quasiparticle and atomic propagation. This delay time is shown in Fig. 6 for  $^{55}\text{Fe}$  events with a variety of fill heights,  $h$ . Here we apply selections on the baseline, delay time, general  $\chi^2$ ,  $\Delta\chi^2$ , and two-pulse-fit  $\chi^2$ , together with a loose selection on the  $^{55}\text{Fe}$  region of Fig. 5. At each fill height an overdensity is evident at the longest delay times, representing the bottom of the  $^4\text{He}$  target region. This is the result of Auger electrons from the source, which exhibit a dramatically shorter path-length in the  $^4\text{He}$ .

At the lowest fill levels the time delay is dominated by atomic propagation through the vacuum state, and we can estimate that atomic velocity scale as  $v_{\text{atom}} = \sim 30$  mm/250  $\mu\text{s} = \sim 100$  m/s. At higher fill levels the quasiparticle state accounts for more of the path length. As the quasiparticle state is faster than the atomic state, this shifts delay time distributions to smaller values. Additionally, as more interaction depths become possible the time delay distribution widens. To estimate the quasiparticle velocity we consider the state where quasiparticles make up the most path length:  $h = 27.7$  mm. In this state the top of the liquid appears at a delay time of  $\sim 40$   $\mu\text{s}$ , and the bottom ap-

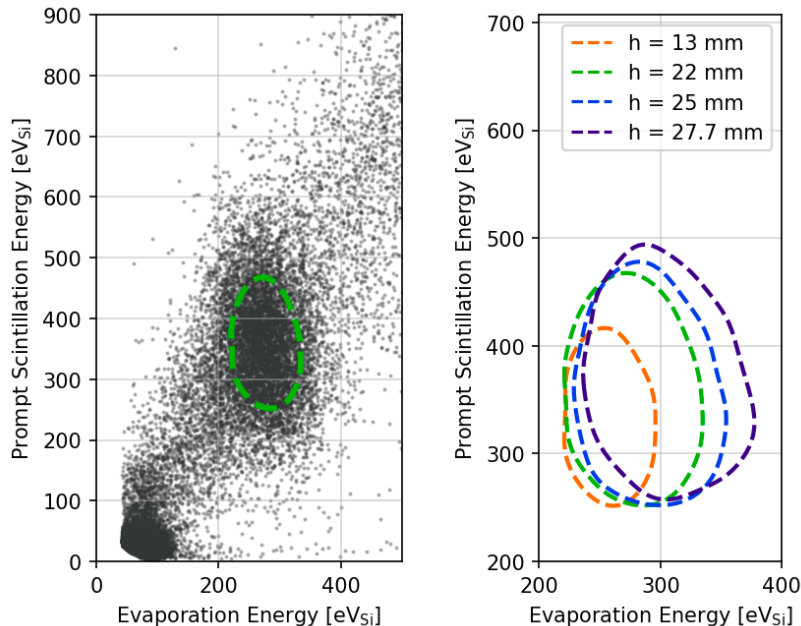


FIG. 5. Distributions of prompt scintillation versus evaporation signal amplitudes. The left panel shows data from the 22 mm fill height. The 5.9 keV  $^{55}\text{Fe}$  peak is highlighted. The right panel shows  $^{55}\text{Fe}$  contours in the plane for multiple  $^4\text{He}$  fill heights. See text for discussion.

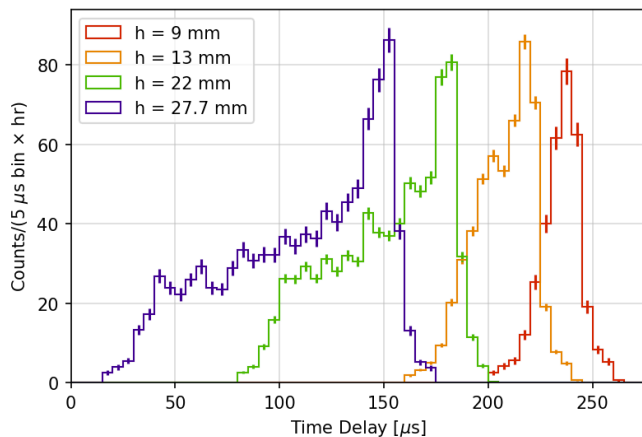


FIG. 6. Evaporation delay time distributions for  $^{55}\text{Fe}$  events. The delay time depends on interaction depth, with the bottom of the detector appearing at the longest delay times (of each fill state).

pears at  $\sim 150 \mu\text{s}$ , implying a quasiparticle velocity of  $v_{\text{qp}} = \sim 27.7 \text{ mm}/110 \mu\text{s} = \sim 250 \text{ m/s}$ . The  $^4\text{He}$  quasiparticle velocity is highly momentum dependent, and this observed velocity implies that the evaporation process is dominated by the fastest quasiparticle states ( $\text{R}^+$  rotons), consistent with expectation.

#### D. Amplitude Variations with Depth

With event depth information from delay time, we can combine the amplitude analysis with delay time to understand how signal efficiency depends on event depth within the  $^4\text{He}$ . Figure 7 shows the evaporation and prompt scintillation energies as functions of delay time for the  $h = 22 \text{ mm}$  fill state. Note that the delay time has been inverted to afford a more intuitive orientation (the bottom of the  $^4\text{He}$  volume is at the bottom of the plot). In this analysis we apply selections on the baseline parameters and  $\Delta\chi^2$ , and we require a scintillation pulse amplitude greater than  $65 \text{ eV}_{\text{Si}}$ . The 5.9 keV population is clearly visible at all delay values (all depths), while the near-threshold 1.5 keV population is visible only very close to the X-ray source itself (due to its short mean-free-path), near the bottom of the  $^4\text{He}$  volume.

The variation of the 5.9 keV signal with depth provides further insight into the physics of the two channels. In the right panel of Fig. 7 the scintillation signal is seen to decrease with distance from the calorimeter, matching expectation from decreasing sensor solid angle. In the left panel the opposite trend with depth appears in the evaporation signal: evaporation signals are larger for interactions occurring deeper within the  $^4\text{He}$ . This counter-intuitive position dependence can be explained by considering those quasiparticles which are emitted from the interaction site but are initially outside the narrow evaporation critical angle previously mentioned. If this much larger quasiparticle population has some probability for

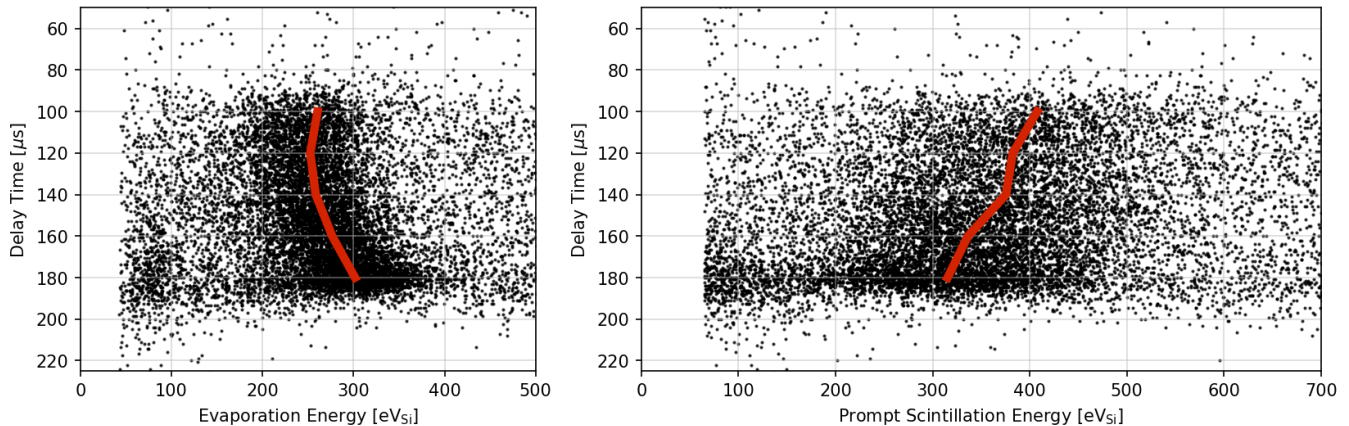


FIG. 7. Evaporation (left) and scintillation (right) signal amplitudes as a function of evaporation delay time, a proxy for event depth within the  ${}^4\text{He}$ . Fill height for this data was  $h = 22$  mm. The main band results from 5.9 keV  ${}^{55}\text{Fe}$  X-rays. The 1.5 keV aluminum fluorescence can be seen near threshold and at the bottom of the active region (bottom left of the plots). Red lines indicate the peak of the  ${}^{55}\text{Fe}$  population, measured with a Gaussian kernel density estimator in 20  $\mu\text{s}$  bins.

diffuse reflection at interfaces, then these diffusely reflected quasiparticles have some probability to then fall within the evaporation critical angle and contribute to the signal. The evaporation signal can thus be broken into two contributions: a ‘primary’ contribution made of quasiparticles which propagate directly to the liquid surface within the critical angle, and a ‘secondary’ contribution made of quasiparticles which evaporate after one or more reflections. The primary contribution will be nearly depth-independent. The secondary contribution will increase in amplitude with depth, as the combined solid angle of the bottom and side walls is larger for deeper positions. The scale of the effect in the left panel of Fig. 7 is consistent with a quasiparticle reflection probability at metal surfaces of  $\sim 0.3$ , consistent with previous literature [17]. The ‘primary’ contribution would then represent a depth-independent  $\sim 200$  eV $_{\text{Si}}$  signal and the ‘secondary’ contribution would represent a boost of  $\sim 20\%$  at the top and  $\sim 40\%$  at the bottom. As mentioned in Sec. IV A, the presence of reflection quasiparticles is further supported by the ‘echo’ features in Fig. 4. Additionally, we highlight a small increase in quasiparticle detection efficiency at the top of the detector (100-120  $\mu\text{s}$ ). This could indicate that a larger fraction of the quasiparticles from near-surface events are evaporating from near the center of the target surface (the intersection of the critical cone and the superfluid surface is narrower), and these quasiparticles have greater solid angle to the sensor.

### E. Triplet Signals

As visible in Fig. 3, times following the evaporation signal are dominated by the deexcitation of long-lived triplet excimers. At high isotopic purity and  $T < 100$  mK, the

long-lived triplet excimers propagate ballistically from the interaction site to the  ${}^4\text{He}$  surfaces. Assuming a velocity of 1-5 m/s [34], we expect propagation times of  $\lesssim 10$  ms in the few-cm  ${}^4\text{He}$  region of this work. Upon arrival at the bottom and sides of the  ${}^4\text{He}$  region, the triplet excimers are expected to promptly decay through electron exchange with the metal. If the triplet excimers instead arrive at the liquid surface, they are expected to diffuse along the surface in a trapped state, until deexcitation can proceed through interaction with another triplet excimer (Penning ionization), a  ${}^3\text{He}$  impurity, or through diffusion all the way to the metal side wall.

Observations of triplet excimer decays are shown in Fig. 8. The left panel shows averaged 5.9 keV waveforms in a long time window, up to 25 ms following the prompt scintillation signal. In this analysis, selections are applied on the baseline quantities, delay time, general  $\chi^2$ , and  $\Delta\chi^2$ . The y-axis unit of eV $_{\text{Si}}$ /ms is scaled from TES current per time using the same calibration factors found previously. It can be seen that, relative to an event occurring in the silicon itself (the red ‘Direct Si Hit’ average),  ${}^4\text{He}$  events exhibit evaporation and then additional signals at later times. At  $t \sim 4$  ms, a ‘shoulder’ appears with depth-dependent amplitude. This few-ms timescale is consistent with that expected for the prompt quenching of excimers directly incident on metal surfaces. At later times, the triplet deexcitation rate follows an exponential decay, with  $\tau \approx 5.4$  ms. This time period may represent the deexcitation of triplets on the liquid surface, and the exponential nature of the process may indicate triplet-triplet deexcitation (for which a  $t^{-1}$  dependence would be expected) is strongly subdominant to other deexcitation mechanisms.

The average energy received by the calorimeter during the triplet-dominated late time window can be found for 5.9 keV deposits by integrating the average waveforms

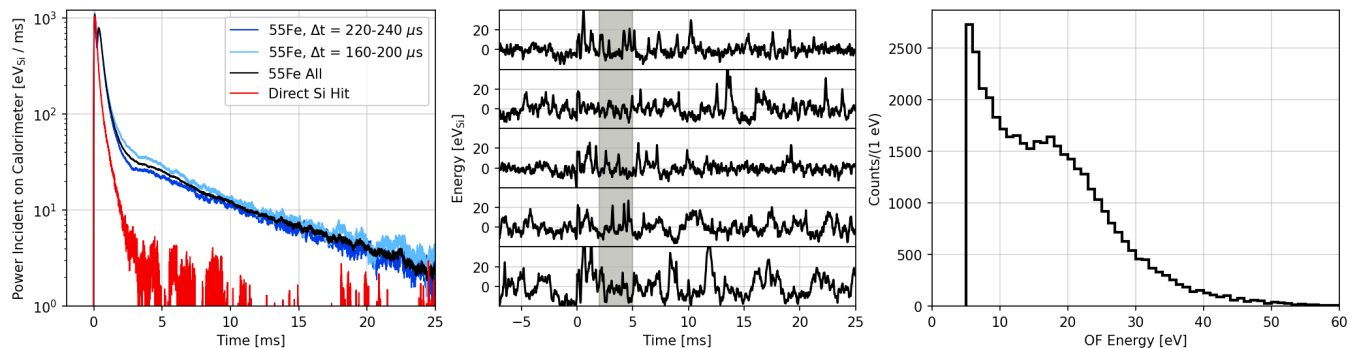


FIG. 8. Observations of triplet excimer decays at late times, using the  $h = 13$  mm data set. *Left*: Waveforms averaged over many  $^{55}\text{Fe}$  events. *Center*: Individual residual waveforms after subtracting the prompt scintillation and evaporation components, revealing small features consistent with individual triplet deexcitations. The grey region indicates the histogram integration window for the right panel. *Right*: A spectrum of the amplitude of the individual small peaks shown in the center panel, indicating rough consistency with the expected 15.5 eV energy.

of Fig. 8 (left). An integral of the 4 ms - 25 ms window corresponds to  $\sim 200$  eV<sub>Si</sub> of received energy. When compared to the  $\sim 320$  eV<sub>Si</sub> prompt scintillation signal at this same  $h = 13$  mm fill state, the triplet deexcitation signal exhibits  $\sim 60\%$  as much energy received. The expected triplet excitation yield in  $^4\text{He}$  is lower than the singlet excitation yield by a factor of  $\sim 0.75$ . After accounting for this difference in yield, the data can be interpreted as implying that the singlet channel “gain” (energy observed per energy excited) is only incrementally higher than the corresponding triplet channel gain.

The middle panel of Fig. 8, shows several typical 5.9 keV waveforms after a procedure to highlight triplet deexcitation features. To construct this version of the event waveforms, the fitted scintillation and evaporation pulses (resulting from the standard two-template OF procedure) are subtracted, leaving a roughly flat residual. This residual waveform is then passed through the scintillation template OF, including the appropriate calibration factor to convert OF amplitude to eV<sub>Si</sub>. In this filtered and energy-calibrated version of the residual waveforms, a number of sharp peaks consistent with individual photon arrivals are evident in the period following  $t=0$ , and the energy of these peaks is seen to be at the expected  $\mathcal{O}(10$  eV<sub>Si</sub>) scale.

The right panel of Fig. 8 shows a histogram of such peak amplitudes. After many 5.9 keV waveforms are passed through the calibrated optimal filtering procedure of the middle panel, the height of all peaks in a  $t = 2$ -5 ms window are tabulated and histogrammed. Noise fluctuations with a standard deviation of 3.2 eV<sub>Si</sub> contribute significantly to population of peaks in this region, and also contribute to a broadening of the observed feature. Gaussian fits have been performed and well describe this peak, but the fitted mean is highly sensitive to the assumed shape of the underlying background and so is not reported. The relatively high value of this peak on the few-ms time-scale (together with the overall high triplet

excimer channel gain factor mentioned earlier) may imply that triplet excimer deexcitations on metal surfaces are sharing only a small fraction of their energy with the copper surfaces, appearing instead as photons of nearly the full 15.5 eV energy.

## V. IMPLICATIONS FOR DARK MATTER SENSITIVITY

The measured evaporation channel gain of  $0.15 \pm 0.012$  allows us to better project future sensitivity of this technology to dark matter detection via nuclear recoils.

We first point out that even at the current R&D stage, we are entering the “quasiparticle-only” signal regime at low energies, where the fraction of recoil energy appearing as electronic excitation is either negligible or truly zero. For this present data, the 5 sigma detection threshold for energy in the  $^4\text{He}$  quasiparticle system is approximately 145 eV. A 145 eV nuclear recoil has some chance of producing a single singlet or triplet excimer (see Ref. [15, 30]), but most nuclear recoils at this energy will convert all recoil energy into a population of quasiparticles of equal total energy. Further, the momentum distribution of quasiparticles is expected to vary only weakly with recoil energy [35], and so expect a similar small variation in evaporation channel gain with recoil energy.

An evaporation channel gain of less than 1 means the recoil energy threshold in  $^4\text{He}$  is currently weaker than the threshold in the calorimeter itself. However, the lower-mass  $^4\text{He}$  nucleus ( $A = 4$ ) boosts the DM recoil energy in  $^4\text{He}$  relative to Si ( $A = 28$ ) by a factor of  $28 / 4 = 7$ , coincidentally similar and countering the low evaporation channel gain:  $0.15 \times 7 = 1.05$ . More succinctly: for the observed quantum evaporation gain of 0.15, the DM mass threshold in the  $^4\text{He}$  and the Si are nearly equal.

A nuclear recoil energy threshold can be translated to a simple estimate for DM mass threshold by assuming a DM velocity equal to the conventional escape velocity of  $v_{esc} = 544$  km/s plus the local standard of rest velocity  $v_0 = 238$  km/s [36]. The current 145 eV energy threshold then implies a current sensitivity to dark matter candidates with  $m_{DM} \gtrsim 220$  MeV/ $c^2$ .

In future work, the calorimeter energy threshold can be significantly reduced. With a heat-free film-stopping method demonstrated, the TES transition temperature can be reduced to less than 20 mK, and such devices have already been fabricated and demonstrated within the SPICE/HeRALD collaboration. Calorimeter energy thresholds of less than 1 eV are expected.

It is reasonable to also expect an increase in the evaporation gain factor in the near term. First, the van der Waals gain (energy per adsorbed atom) can be increased by moving away from Si to alternative calorimeter substrates which more strongly polarize the  $^4\text{He}$  atom upon arrival. For example, an  $\text{Al}_2\text{O}_3$  (sapphire) substrate is expected to increase the van der Waals adsorption energy by a factor of  $\sim 2$  [37], and successful device fabrication on  $\text{Al}_2\text{O}_3$  has already been demonstrated within the SPICE/HeRALD collaboration. Second, while this current work demonstrates some small increase in gain from quasiparticle reflection at material interfaces, a moderate increase in quasiparticle reflection probability (through alternative coatings of detector surfaces) would result in a faster-than-linear increase in the evaporation probability after multiple reflections.

For illustrative purposes, we project the sensitivity of a near-term HeRALD experiment with moderate improvement in each aspect. If one assumes a calorimeter energy threshold of  $\sim 1$  eV, a  $\sim 2\times$  increase in van der Waals gain, and a  $\sim 2\times$  increase in evaporation efficiency (a combined gain factor of  $0.15 \times 2 \times 2 = 0.6$ ), then the resulting a  $^4\text{He}$  nuclear recoil energy threshold would be  $\sim 1$  eV/ $0.6 = \sim 1.7$  eV and the dark matter mass threshold would be  $m_{DM} \gtrsim 30$  MeV/ $c^2$ .

## VI. CONCLUSIONS

We have presented the design and first results of an initial  $^4\text{He}$  test detector, ‘HeRALD v0.1’. The main goals of this R&D phase were to determine the efficacy of the cesium film-stopping system and to make first observations of particle interactions in the superfluid  $^4\text{He}$  target. These studies show that the cesium film-stopping system can be made practical, and that it is effective over the course of a multiple-week operation.

The newly-measured evaporation channel gain of  $0.15 \pm 0.012$  is sufficient for interesting DM sensitivity in the near term after transitioning to lower-energy-threshold calorimetry. The existing gain factor results in DM mass thresholds similar to the Si calorimeter itself. Future improvement in this gain factor is expected through both increased van der Waals adsorption ener-

gies and increased  $^4\text{He}$  quasiparticle reflection probabilities.

We also highlight the importance of the newly observed triplet excimer deexcitation timescale. The long triplet excimer lifetime in the bulk has implied that these excimers could potentially form a background of eV-scale ‘dark counts’ in a future DM search. The newly observed high triplet signal gain and few-ms exponential decay timescale suggests that these excimers are largely removed on short timescales.

This is only a first demonstration of the HeRALD architecture. We anticipate a significant reduction in energy threshold, giving HeRALD a path to probing DM masses at or below 30 MeV/ $c^2$  within a small number of years.

## ACKNOWLEDGMENTS

We would like to thank Maryvonne De Jesus for providing the  $^{55}\text{Fe}$  source used in these studies. Additionally, we would like to thank George Seidel for useful conversations throughout the course of this work. H.D.P would like to thank the hospitality of the MANOIR group at the IP2I in Lyon where a portion of this analysis was performed during a stay funded in part by the Chateaubriand Fellowship. This work was supported in part by DOE Grants DE-SC0019319 and DE-SC0022354, and DOE Quantum Information Science Enabled Discovery (QuantISED) for High Energy Physics (KA2401032). This material is based upon work supported by the National Science Foundation Graduate Research Fellowship under Grant No. DGE 1106400. This material is based upon work supported by the Department of Energy National Nuclear Security Administration through the Nuclear Science and Security Consortium under Award Number(s) DE-NA0003180 and/or DE-NA0000979. Work at Argonne is supported by the U.S. DOE, Office of High Energy Physics, under Contract No. DE-AC02-06CH11357. Work at Lawrence Berkeley National Laboratory is supported by the U.S. DOE, Office of High Energy Physics, under Contract No. DE-AC02-05CH11231. W.G. and Y.Q. acknowledge the support by the National High Magnetic Field Laboratory at Florida State University, which is supported by the National Science Foundation Cooperative Agreement No. DMR-2128556 and the state of Florida.

## Appendix A: Cryostat Systems

The dilution refrigerator used for this study is a CryoConcept Hexadry UQT-B 400. Figure 9 schematically illustrates the routing of several components through the cryostat to the cell: a capillary for both filling and removing  $^4\text{He}$ , high-current leads for cesium evaporation, and a DC SQUID readout chain for the TES sensor.

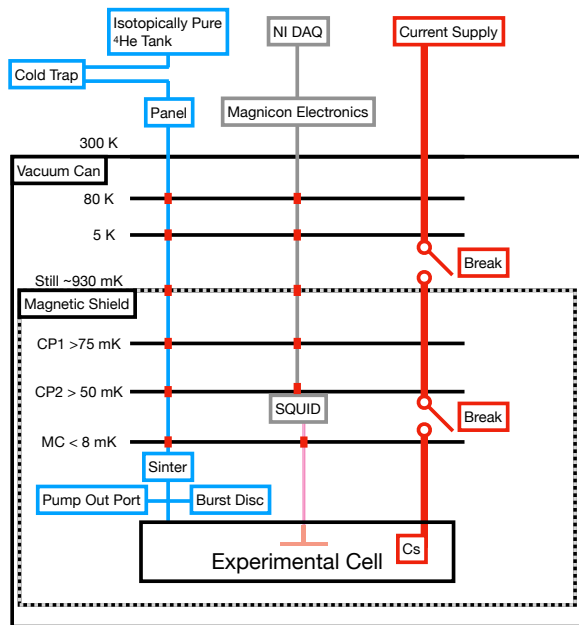


FIG. 9. Schematic of experimental subsystems within the dilution refrigerator. Shown in blue is the isotopically-pure  $^4\text{He}$  injection system. The Magnicon SQUID readout is shown in grey, the sensor is shown in orange, and the NbTi twisted-pair connections between the SQUID and sensor are shown in pink. The  $^4\text{He}$  and readout systems are heat-sunk at each thermal stage, represented by red blocks in-line with the readout. Finally, the cesium dispensing system is shown as a thick red line with switches representing the post-evaporation break points just above the still and mixing chamber (MC) stages. Thermal shields at 80 K and 5 K are not shown. The shield at the Still is made of Cryoperm and doubles as a magnetic shield.

### 1. $^4\text{He}$ Handling System

The capillary system carries  $^4\text{He}$  from room temperature storage to the experimental cell. The  $^4\text{He}$  itself was isotopically enriched at Lancaster University<sup>2</sup> with a  $^3\text{He}$  concentration below  $5 \times 10^{-13}$  [38]. At room temperature the  $^4\text{He}$  is stored in a large low-pressure ( $\sim 1$  atm) storage vessel. A gas handling system can circulate the  $^4\text{He}$  through a liquid-nitrogen cooled activated-charcoal cold-trap. During filling a mass flow controller (MFC) is used to regulate the  $^4\text{He}$  condensation. To preserve  $^4\text{He}$  purity, all connections are either welded or VCR (metal gasket). The only exception to this design philosophy was a ceramic electrical break near the refrigerator flange which was mated using Swagelok compression fittings.

The  $^4\text{He}$  connection between room-temperature and the 80 K stage of the refrigerator was made with a 1/4" VCR-flanged flexible bellows. This bellows accommo-

dates thermal contractions during the cooldown and provides moderate surface area for any impurities which escape the cold-trap. Below the 80 K stage the  $^4\text{He}$  is carried through a stainless steel capillary (2.1 mm OD, 1.7 mm ID). At each temperature stage, including 80 K, this line is heat-sunk by breaking the capillary and soldering the ends into a copper block with a large (4 mm ID) bore. The  $^4\text{He}$  line connects to the cell through a  $0.5 \mu\text{m}$  sinter, intended both to dampen any thermo-acoustic oscillations during filling and also to prevent any flow of gas atoms from the warmer stages to the cell interior during data-taking. The cell and capillary are typically pumped out via a copper pinch-off tube mounted at the top of the cell (however, the pinch-off tube was not used in this experiment and the cell was only evacuated through the capillary). In case of a capillary blockage or a sudden temperature rise, the cell is fitted with a burst disc and the fridge vacuum volume is fitted with a pressure relief valve.

### 2. Film Stopping and the Cesium System

The HeRALD collaboration considered two techniques of film stopping: the knife-edge and cesium methods.

The knife-edge method, demonstrated at higher temperatures (particularly by X-ray observing satellites [39–41]), interrupts film flow using an extremely sharp corner separating the bulk  $^4\text{He}$  and the film-free region. The van der Waals attraction of the  $^4\text{He}$  to the knife edge material forces the film to thin in the vicinity of the edge. For a sufficiently sharp edge, the film can be thinned below its critical thickness such that the film will no longer exhibit superflow. However, this critical film thickness decreases with temperature, such that for the  $\sim 10$  mK temperature of HeRALD superflow can appear in films as thin as 2.1 atomic layers [42–44]. This nearly-atomic critical film thickness requires a near-atomically-sharp knife edge (a radius of curvature at or below the nanometer scale [40, 41, 45]). We investigated fabrication of such devices through anisotropic etching of Si, and achieved knife edge radii only as low as  $\sim 7$  nm. Given the challenges of this technique and the promise of the cesium method, the knife edge development was discontinued.

The mechanism of the cesium method was described in Sec. IB. The evaporation system used to implement this method must overcome several technical challenges stemming from cesium’s extreme reactivity and high vapor pressure [46]. The substrate for cesium deposition is gold-plated to reduce that substrate’s cesium reactivity. To avoid oxidation, the cesium is evaporated directly onto the desired surfaces within the cell, after it is mounted on the mixing chamber, and after cooling the mixing chamber stage and cell to  $\sim 4$  K. Cesium is evaporated from the dispensers towards the gold-plated substrate, and copper baffling prevents cesium from entering the experimental area below. The required 7.5 A evaporation current is delivered via  $\sim 1$  mm diameter Kapton-insulated copper

<sup>2</sup> <https://www.lancasterhelium.uk/>

wire. This cabling would represent a significant heat load to the coldest stages of the refrigerator, and so this heat load is eliminated using “breaks” in the current leads just above the mixing chamber and still stages. At these breaks, the copper wire is pressed between copper (grade 101) spring clamps. At room temperature a linear direct mechanical feed-through can be manipulated after cesium deposition in order to open the two thermal breaks. This manipulation also engages an electrical grounding spring to the cesium leads at the mixing chamber stage to mitigate electrical noise pickup.

### 3. Detector Readout

The final detector system is a DC SQUID from Magnicon for TES readout. The TES array is connected to the 16-SQUID series array using a superconducting NbTi wire twisted pair, in parallel with a 2 m $\Omega$  shunt resistor patterned onto the Magnicon SQUID chip itself. The SQUID is shielded magnetically by a superconducting Nb can around the array, and the entire low-temperature readout is surrounded by a magnetic shield which doubles as our still stage thermal shield. The SQUID array is controlled at room temperature with an XXF-1 elec-

tronics system. Signals are filtered with a 500 kHz low-pass anti-aliasing filter, and recorded at 1.25 MHz using a National Instruments PCI-e 6376 data acquisition card controlled by the `polaris` package [47], wrapped within `pytesdaq` [48].

### Appendix B: Detector Preparation

Prior to the data-taking, we first prepare the cell and cesium film. This begins at room temperature by evacuating the cell to at least  $\sim 10^{-4}$  mbar. While continuing to pump we outgas the cesium dispensers (ramping up to 3 A, in 10-minute steps of 1 A), raising the dispenser temperature to  $\sim 400$  °C [49]. After returning to base pressure, we end the pumping. Once the refrigerator is cooled to  $\sim 4$  K, we perform the cesium evaporation procedure (ramping up to 7.5 A, in 10-minute steps of 1 A). After holding for 20 minutes at 7.5 A (a dispenser temperature of  $\sim 800$  °C), the majority of cesium has been evaporated and the current is stopped. This procedure heats the sensor platform to approximately 70 K. Following the evaporation we disconnect the cesium leads with the breaks and mechanical feedthrough described in Appendix A and cool the refrigerator to base temperature.

- 
- [1] E. Kuflik, M. Perelstein, N. R.-L. Lorier, and Y.-D. Tsai, Elastically Decoupling Dark Matter, *Physical Review Letters* **116**, 221302 (2016).
  - [2] E. Kuflik, M. Perelstein, N. R.-L. Lorier, and Y.-D. Tsai, Phenomenology of ELDER dark matter, *Journal of High Energy Physics* **2017**, 78 (2017).
  - [3] Y. Hochberg, E. Kuflik, T. Volansky, and J. G. Wacker, Mechanism for Thermal Relic Dark Matter of Strongly Interacting Massive Particles, *Physical Review Letters* **113**, 171301 (2014).
  - [4] Y. Hochberg, E. Kuflik, H. Murayama, T. Volansky, and J. G. Wacker, Model for Thermal Relic Dark Matter of Strongly Interacting Massive Particles, *Physical Review Letters* **115**, 021301 (2015).
  - [5] L. J. Hall, K. Jedamzik, J. March-Russell, and S. M. West, Freeze-in production of FIMP dark matter, *Journal of High Energy Physics* **2010**, 80 (2010).
  - [6] D. McKinsey, Snowmass 2021 - Letter of Interest. The TESSERACT Dark Matter Project.
  - [7] P. Adari *et al.*, EXCESS workshop: Descriptions of rising low-energy spectra, *SciPost Physics Proceedings*, 001 (2022).
  - [8] R. Anthony-Petersen *et al.*, A Stress Induced Source of Phonon Bursts and Quasiparticle Poisoning (2022), arxiv:2208.02790 [cond-mat, physics:physics].
  - [9] J. Åström *et al.*, Fracture processes observed with a cryogenic detector, *Physics Letters A* **356**, 262 (2006).
  - [10] G. Angloher *et al.* (CRESST), Latest observations on the low energy excess in CRESST-III (2022), arxiv:2207.09375 [astro-ph].
  - [11] G. Vidali, G. Ihm, H.-Y. Kim, and M. W. Cole, Potentials of physical adsorption, *Surface Science Reports* **12**, 135 (1991).
  - [12] Daniel Nicholas McKinsey, *Detection of Magnetically Trapped Neutrons: Liquid Helium as a Scintillator*, Ph.D. thesis, Harvard University (2002).
  - [13] D. N. McKinsey, C. R. Brome, S. N. Dzhosyuk, R. Golub, K. Habicht, P. R. Huffman, E. Korobkina, S. K. Lamoreaux, C. E. H. Mattoni, A. K. Thompson, L. Yang, and J. M. Doyle, Time dependence of liquid-helium fluorescence, *Physical Review A* **67**, 062716 (2003).
  - [14] D. N. McKinsey, C. R. Brome, J. S. Butterworth, S. N. Dzhosyuk, P. R. Huffman, C. E. H. Mattoni, J. M. Doyle, R. Golub, and K. Habicht, Radiative decay of the metastable He<sub>2</sub>(a<sup>3</sup>Σ<sub>u</sub><sup>+</sup>) molecule in liquid helium, *Physical Review A* **59**, 200 (1999).
  - [15] S. A. Hertel, A. Biekert, J. Lin, V. Velan, and D. N. McKinsey, Direct detection of sub-GeV dark matter using a superfluid <sup>4</sup>He target, *Physical Review D* **100**, 092007 (2019).
  - [16] R. E. Lanou, H. J. Maris, and G. M. Seidel, Detection of solar neutrinos in superfluid helium, *Physical Review Letters* **58**, 2498 (1987).
  - [17] S. R. Bandler, R. E. Lanou, H. J. Maris, T. More, F. S. Porter, G. M. Seidel, and R. H. Torii, Particle detection by evaporation from superfluid helium, *Physical Review Letters* **68**, 2429 (1992).
  - [18] J. S. Adams, S. R. Bandler, S. M. Brouer, C. Enss, R. E. Lanou, H. J. Maris, T. More, and G. M. Seidel, ‘HERON’ as a dark matter detector?, in *31st Rencontres de Moriond: Dark Matter and Cosmology, Quantum Measurements and Experimental Gravitation* (1996) pp. 131–136.

- [19] Frank Pobell, *Matter and Methods at Low Temperatures*, 3rd ed. (Springer Berlin, Heidelberg, 2007).
- [20] M. J. Baird, F. R. Hope, and A. F. G. Wyatt, Quantized evaporation from liquid helium, *Nature* **304**, 325 (1983).
- [21] R. Torii, S. R. Bandler, T. More, F. S. Porter, R. E. Lanou, H. J. Maris, and G. M. Seidel, Removal of superfluid helium films from surfaces below 0.1 K, *Review of Scientific Instruments* **63**, 230 (1992).
- [22] E. Cheng, M. W. Cole, W. F. Saam, and J. Treiner, Helium prewetting and nonwetting on weak-binding substrates, *Physical Review Letters* **67**, 1007 (1991).
- [23] K. S. Ketola, S. Wang, and R. B. Hallock, Anomalous wetting of helium on cesium, *Physical Review Letters* **68**, 201 (1992).
- [24] P. J. Nacher and J. Dupont-Roc, Experimental evidence for nonwetting with superfluid helium, *Physical Review Letters* **67**, 2966 (1991).
- [25] J. E. Rutledge and P. Taborek, Prewetting phase diagram of  $^4\text{He}$  on cesium, *Physical Review Letters* **69**, 937 (1992).
- [26] C. W. Fink *et al.* (CPD Collaboration), Performance of a large area photon detector for rare event search applications, *Applied Physics Letters* **118**, 022601 (2021).
- [27] I. Alkhatib *et al.* (SuperCDMS Collaboration), Light Dark Matter Search with a High-Resolution Athermal Phonon Detector Operated above Ground, *Physical Review Letters* **127**, 061801 (2021).
- [28] K. D. Irwin, S. W. Nam, B. Cabrera, B. Chugg, and B. A. Young, A quasiparticle-trap-assisted transition-edge sensor for phonon-mediated particle detection, *Review of Scientific Instruments* **66**, 5322 (1995).
- [29] H. D. Pinckney, G. Yacteen, A. Serafin, and S. A. Hertel, The Thermal Conductance of Sapphire Ball Based Detector Clamps, *Journal of Low Temperature Physics* **209**, 1204 (2022).
- [30] A. Biekert *et al.* (SPICE/HeRALD Collaboration), Scintillation yield from electronic and nuclear recoils in superfluid  $^4\text{He}$ , *Physical Review D* **105**, 092005 (2022), arxiv:2108.02176 [astro-ph, physics:hep-ex, physics:physics].
- [31] M. Szydagis *et al.*, Noble element simulation technique (2023).
- [32] M. Szydagis *et al.*, A Review of NEST Models, and Their Application to Improvement of Particle Identification in Liquid Xenon Experiments (2023), arxiv:2211.10726 [astro-ph, physics:hep-ex, physics:nuc-ex, physics:physics].
- [33] K. Irwin and G. Hilton, Transition-Edge Sensors, in *Cryogenic Particle Detection*, Topics in Applied Physics, edited by C. Enss (Springer, Berlin, Heidelberg, 2005) pp. 63–150.
- [34] D. E. Zmeev, F. Papkour, P. M. Walmsley, A. I. Golov, P. V. E. McClintock, S. N. Fisher, W. Guo, D. N. McKinsey, G. G. Ihas, and W. F. Vinen, Observation of Crossover from Ballistic to Diffusion Regime for Excimer Molecules in Superfluid  $^4\text{He}$ , *Journal of Low Temperature Physics* **171**, 207 (2013).
- [35] Y. You, J. Smolinsky, W. Xue, K. T. Matchev, K. Gunther, Y. Lee, and T. Saab, Signatures and Detection Prospects for sub-GeV Dark Matter with Superfluid Helium (2022), arxiv:2208.14474 [astro-ph, physics:cond-mat, physics:hep-ex, physics:hep-ph].
- [36] D. Baxter *et al.*, Recommended conventions for reporting results from direct dark matter searches, *The European Physical Journal C* **81**, 907 (2021), arxiv:2105.00599 [hep-ex, physics:hep-ph].
- [37] G. Zhang, X. Xiang, F. Yang, L. Liu, T. Tang, Y. Shi, and X. Wang, First principles investigation of helium physisorption on an  $\alpha\text{-Al}_2\text{O}_3$  (0001) surface, *Physical Chemistry Chemical Physics* **18**, 15711 (2016).
- [38] P. C. Hendry and P. V. E. McClintock, Continuous flow apparatus for preparing isotopically pure  $^4\text{He}$ , *Cryogenics* **27**, 131 (1987).
- [39] Y. Ezoe *et al.*, Porous plug phase separator and superfluid film flow suppression system for the soft x-ray spectrometer onboard Hitomi, *Journal of Astronomical Telescopes, Instruments, and Systems* **4**, 011203 (2017).
- [40] K. Ishikawa *et al.*, Porous plug and superfluid helium film flow suppressor for the soft X-ray spectrometer onboard Astro-H, *Cryogenics 2009 Space Cryogenic Workshop*, **50**, 507 (2010).
- [41] P. J. Shirron and M. J. DiPirro, Suppression of Superfluid Film Flow in the XRS Helium Dewar, in *Advances in Cryogenic Engineering*, Advances in Cryogenic Engineering, edited by P. Kittel (Springer US, Boston, MA, 1998) pp. 949–956.
- [42] M. H. W. Chan, A. W. Yanof, and J. D. Reppy, Superfluidity of thin  $^4\text{He}$  films, *Physical Review Letters* **32**, 1347 (1974).
- [43] J. H. Scholtz, E. O. McLean, and I. Rudnick, Third Sound and the Healing Length of He II in Films as Thin as 2.1 Atomic Layers, *Physical Review Letters* **32**, 147 (1974).
- [44] D. F. Brewer, A. J. Symonds, and A. L. Thomson, Gapless Surface Excitations in Liquid Helium, *Physical Review Letters* **15**, 182 (1965).
- [45] P. V. E. McClintock, Thickness of the helium film on a curved substrate, *Physics Letters A* **46**, 145 (1973).
- [46] Oswald Kubaschewski, Elwyn Llewellyn Evans, and C. B. Alcock, *Metallurgical Thermochemistry*, 4th ed. (Pergamon Press, Oxford, 1967).
- [47] B. Suerfu, Polaris: A general-purpose, modular data acquisition framework, *Journal of Instrumentation* **13** (12), T12004.
- [48] Pytesdaq, SPICE/HeRALD GitHub (2022).
- [49] P. della Porta, C. Emili, and S. J. Hellier, *Alkali Metal Generation and Gas Evolution from Alkali Metal Dispensers*, Tech. Rep. Technical Report TR 18.